ARTICLE

Check for updates

Parallel detection and spatial mapping of large nuclear spin clusters

K. S. Cujia [1,3 ✉], K. Herb[1 ✉], J. Zopes[1,4 ✉], J. M. Abendroth[1 ✉] & C. L. Degen [1,2 ✉]

Nuclear magnetic resonance imaging (MRI) at the atomic scale offers exciting prospects for determining the structure and function of individual molecules and proteins. Quantum defects in diamond have recently emerged as a promising platform towards reaching this goal, and allowed for the detection and localization of single nuclear spins under ambient conditions. Here, we present an efficient strategy for extending imaging to large nuclear spin clusters, fulfilling an important requirement towards a single-molecule MRI technique. Our method combines the concepts of weak quantum measurements, phase encoding and simulated annealing to detect three-dimensional positions from many nuclei in parallel. Detection is spatially selective, allowing us to probe nuclei at a chosen target radius while avoiding interference from strongly-coupled proximal nuclei. We demonstrate our strategy by imaging clusters containing more than 20 carbon-13 nuclear spins within a radius of 2.4 nm from single, near-surface nitrogen–vacancy centers at room temperature. The radius extrapolates to 5–6 nm for ^{1}H. Beside taking an important step in nanoscale MRI, our experiment also provides an efficient tool for the characterization of large nuclear spin registers in the context of quantum simulators and quantum network nodes.

[1] Department of Physics, ETH Zurich, Otto Stern Weg 1, 8093 Zurich, Switzerland. [2] Quantum Center, ETH Zurich, 8093 Zurich, Switzerland. [3] Present address: IT'IS Foundation, Zeughausstrasse 43, 8004 Zurich, Switzerland. [4] Present address: Ansys Switzerland GmbH, Technoparkstrasse 1, 8005 Zurich, Switzerland. ✉email: cujiapek@phys.ethz.ch; kh@rashbw.de; jonathanzopes@gmail.com; jabendroth@phys.ethz.ch; degenc@ethz.ch

Nuclear magnetic resonance (NMR) spectroscopy and magnetic resonance imaging (MRI) are powerful tools for molecular analysis and medical diagnostics. While conventional NMR operates on millimeter-sized samples containing large ensembles of molecules, much effort has been directed toward improving the resolution to the nanometer scale[1,2] where the atomic structure could be analyzed at the level of individual molecules[3]. Such a "single-molecule MRI" technique would enable direct imaging of molecular structures with three-dimensional resolution and elemental specificity[1] and the monitoring of chemical reactions and binding[4,5]. This capability could lead to many applications in biology, chemistry, and nanosciences, especially because MRI avoids important limitations of other structural techniques (like X-ray diffraction or electron microscopy) such as radiation damage and the need for ensemble averaging[6,7].

Quantum sensors based on nitrogen-vacancy (NV) centers in diamond have recently generated exciting progress in micronscale[8,9] and nanoscale[10–12] NMR spectroscopy. Early experiments have demonstrated the detection of single nuclear spins within the diamond crystal[13–15] as well as of nanoscale films deposited on diamond surfaces[10–12,16]. A recent refinement of protocols has led to tremendous advances in sensitivity and spectral resolution[8,17,18], allowing for the three-dimensional localization of individual nuclear spins[19–22], spin pairs[23–25], and the chemical fingerprinting of molecular ensembles with high spectral resolution[8,26]. Most recently, Abobeih et al.[27] reported the milestone achievement of a complete mapping of a 27-nuclear-spin cluster at cryogenic temperatures.

To extend experiments to the imaging of single molecules, approaches are needed that are compatible with near-surface NV centers ($\lesssim 5$ nm) and preferably an ambient environment. Moreover, methods are required that can efficiently detect and precisely localize a large number of distant nuclear spins in parallel. While advanced strategies have been developed to solve the latter challenge of nuclear spin detection and localization[27–32], many of these strategies require very long coherence times or a single-shot readout of the quantum sensor to reach adequate sensitivity and spectral resolution[27,33]. These conditions are difficult to realize with shallow defect centers at room temperature[34,35].

In this work, we demonstrate a powerful method for the sensitive detection and spatial mapping of individual nuclei in large nuclear spins clusters. Our approach combines the concepts of weak quantum measurements[36,37], phase encoding[21,22], and simulated annealing[38,39] to detect signals and extract precise three-dimensional distances from many nuclei in parallel. We further show that our detection is spatially selective, allowing us to probe nuclei at a chosen target radius while avoiding interference from strongly-coupled proximal nuclei. We demonstrate our strategy by mapping the ^{13}C environment of two NV centers containing 20 and 29 nuclei, respectively. Because our experiments are performed on near-surface spin defects and at room temperature, they are compatible with the demanding environment of prospective single-molecule MRI investigations. Besides taking an important step in developing a single-molecule MRI platform, our experiment also provides an efficient tool for the characterization of large qubit registers in the context of quantum simulators[40], quantum network nodes[33,41,42], and multi-qubit quantum processors[43,44].

Results

Imaging concept. Our concept and the experimental situation is sketched in Fig. 1a. We consider a central electronic spin surrounded by a group of nuclear spins whose three-dimensional locations we aim to determine. Here, both the electronic and

nuclear spins are embedded in the solid matrix of a diamond crystal, but our concept is applicable to a general situation of a localized electronic spin[45–47] and a nearby nuclear ensemble, including surface molecules[10,11,48] or crystalline layers[49]. The electronic spin plays a dual role in our arrangement[30]: first, it acts as a local sensor for the weak magnetic fields produced by the nearby nuclei. Second, it generates a strong magnetic dipole field that we exploit for spatial imaging. In a reference frame where z is the common quantization axis (Fig. 1b), the dipole field is given by:

$$\mathbf{a}/\gamma_n = \frac{\mu_0 \hbar \gamma_e m_S}{4\pi r^3} \left[\frac{3\mathbf{r}(\mathbf{e}_z \cdot \mathbf{r})}{r^2} - \mathbf{e}_z \right], \tag{1}$$

where $\mathbf{a}$ is the hyperfine vector (see Fig. 1b), $\mathbf{r} = (r, \vartheta, \phi)$ are the polar coordinates of the nuclear spin relative to the electron spin situated at the origin, $\mathbf{e}_z$ is a unit vector along z, m_S is the magnetic quantum number of the electronic spin ($m_S \in \{-1, 0, 1\}$ for the NV center). Because we will be detecting distant ^{13}C spins, the Fermi contact interaction can be safely neglected[20,50]. Further, μ_0 is the vacuum permeability, $\hbar$ the reduced Planck constant, and γ_e and γ_n are the electronic and nuclear gyromagnetic ratios, respectively. Thus, by measuring the three components of the hyperfine vector $\mathbf{a}$, the distance vector $\mathbf{r}$ can be directly inferred (up to an inversion symmetry at the origin), revealing a spin's three-dimensional spatial location.

Parallel signal acquisition. While this scheme of three-dimensional localization has been demonstrated on individual nuclear spins[19–22], the principal challenge lies in extending these experiments to large numbers of nuclei. We address this challenge by exploiting the principle of weak quantum measurements[36,51], which closely resembles the detection of a free induction decay (FID) signal in canonical Fourier NMR spectroscopy. Figure 2 introduces our experimental protocol, consisting of a polarization, excitation, and read-out step. We begin by hyperpolarizing nuclear spins through a polarization transfer from the optically-aligned electronic spin (Fig. 2a). This initial step, when applied repetitively and for a sufficiently long time, leads to a volume of near-fully polarized nuclei around the central electronic spin[52]. We then excite all nuclei simultaneously using a broad-band $\pi/2$ pulse and detect the free nuclear precession signal by sampling the transverse nuclear magnetization using weak measurements[36]. The procedure yields an FID signal of the form:

$$x(t) = \sum_{i=1}^{n} A(\beta_i) e^{-\Gamma(\beta_i)t} \cos[\omega_i t + \phi_i], \tag{2}$$

where n is the number of nuclear spins. Further, $A(\beta_i)$ is the probability amplitude[17], $\Gamma(\beta_i)$ the dephasing rate, ω_i the precession frequency, and ϕ_i the initial phase of the signal belonging to the i'th nucleus. The parameter:

$$\beta_i = \frac{a_{\perp,i} t_\beta}{\pi} \tag{3}$$

is a "measurement gain" parameter that is proportional to the hyperfine coupling constant $a_{\perp,i}$ multiplied by the interaction time t_β of the ac detection (Fig. 2b). The parameter β_i, discussed in Section V, plays an important role in single-spin FID detection as it governs the balance between signal gain and quantum backaction[36,37,53]. We sample the FID at instances $t = k t_s$, where t_s is the sampling time, $k = 1 \ldots K$, and where K is the number of points in the FID trace (Fig. 2).

Hyperfine parameters. We next show that an FID trace described by Eq. (2) contains all the information needed to reconstruct the hyperfine vectors $\mathbf{a}_i$, and hence, the three-dimensional locations $\mathbf{r}_i$ of the nuclear spins. First, the parallel components $a_{\parallel,i}$ (see
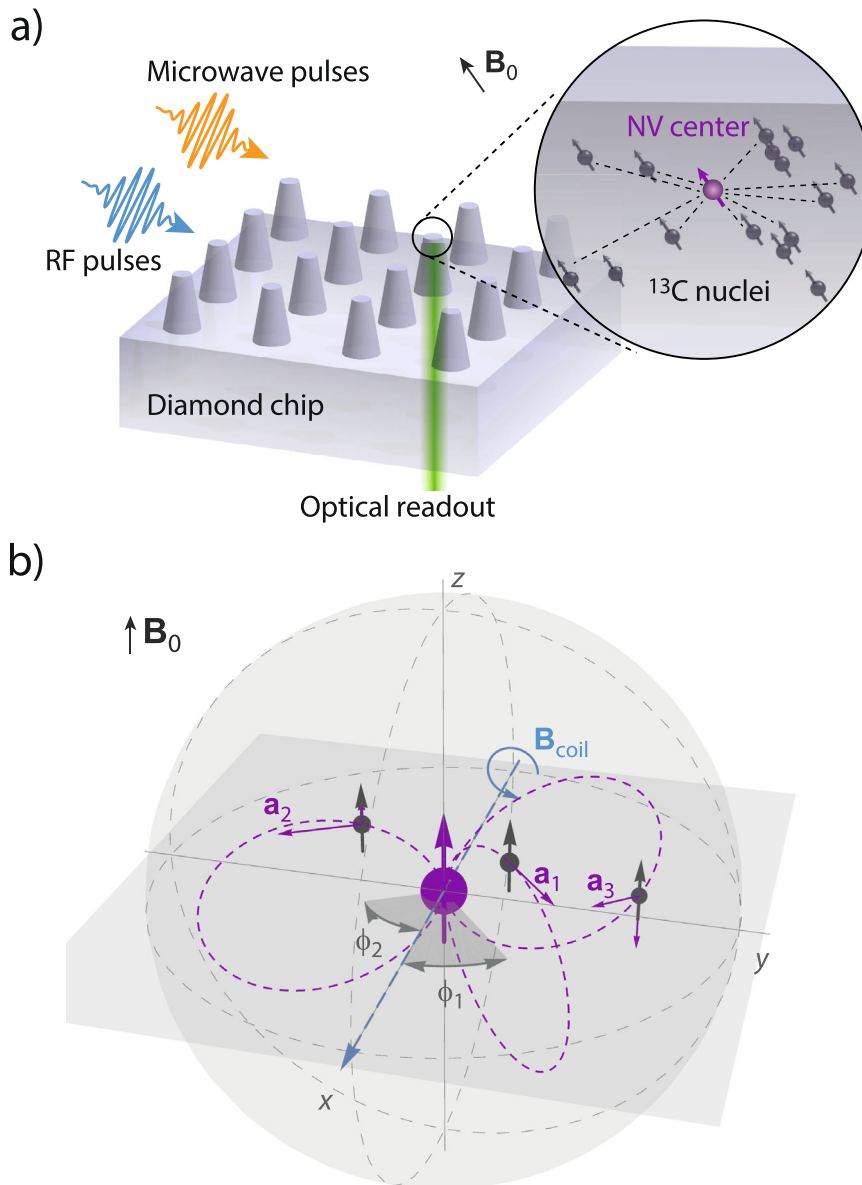
Fig. 1 Concept of the nuclear spin mapping experiment. a We detect and image nuclear spins (black) surrounding a central electronic spin (purple). In our experiments, spins are embedded in a nanostructured diamond chip, manipulated by microwave and radio-frequency (RF) pulses, and detected by optical means. **b** Spatial imaging is enabled through the hyperfine field $\mathbf{a} = (a_\perp \cos\phi, a_\perp \sin\phi, a_{||})$, whose magnitude and direction strongly depend on the three-dimensional position $\mathbf{r} = (r, \vartheta, \phi)$. We determine the radius r and polar angle ϑ by measuring the parallel and transverse hyperfine components, $a_{||,i} = \mathbf{a} \cdot \mathbf{e}_z$ and $a_{\perp,i} = |\mathbf{a} \times \mathbf{e}_z|$[19,54]. The azimuth ϕ is equal to the phase of the nuclear precession[21,22]. $\mathbf{e}_z$ is a unit vector pointing along the electronic quantization axis and $\mathbf{B}_0 || \mathbf{e}_z$ is an external bias field. $\mathbf{B}_{coil} || \mathbf{e}_x$ is the direction of the RF field.

Fig. 1b) can be determined from the spectral positions of the nuclear resonances, given by the free precession frequencies:

$$\omega_i = \frac{1}{2}\left(\omega_0 + \sqrt{(\omega_0 + a_{||,i})^2 + a_{\perp,i}^2}\right) \approx \omega_0 + \frac{1}{2}a_{||,i}, \quad (4)$$

where the approximation is for small $a_{||,i}$, $a_{\perp,i} \ll \omega_0$ (fulfilled in our experiments but not required for the analysis) and where $\omega_0 = -\gamma_n B_0$, with $B_0 || \mathbf{e}_z$ being the external magnetic bias field[54].

The amplitudes $A(\beta_i)$ and decay rates $\Gamma(\beta_i)$ encode information about the perpendicular components $a_{\perp,i}$ (See Supplementary Materials accompanying this manuscript):

$$A(\beta_i) = \frac{1}{2}p_{0,i}\sin(\beta_i) \approx \frac{p_0 a_{\perp,i} t_\beta}{2\pi}, \quad (5a)$$

$$\Gamma(\beta_i) = \frac{a_{\perp,i}^2 t_\beta^2}{4t_s \pi^2} + \frac{a_{||,i}^2 t_\ell^2}{2t_s} + \frac{1}{T_{2,n}^*}, \quad (5b)$$

where $p_{0,i}$ is the initial polarization of the i'th nuclear spin. Note that the $p_{0,i}$ also contain any pulse errors and other imperfections of the pulse sequence, and therefore rather reflect pre-scaling factors and a lower bound for the nuclear polarization. The dephasing rate $\Gamma(\beta_i)$ is influenced by three effects: a measurement-induced dephasing proportional to $a_{\perp,i}^2 t_\beta^2$ due to quantum back-action[36]. (ii) An additional decay rate proportional to $a_{||,i}^2 t_\ell^2$ that is specific to the stochastic optical read-out process of the NV center with effective duration t_ℓ[36]. (iii) An intrinsic $T_{2,i}^*$ decay that accounts for all dephasing mechanisms
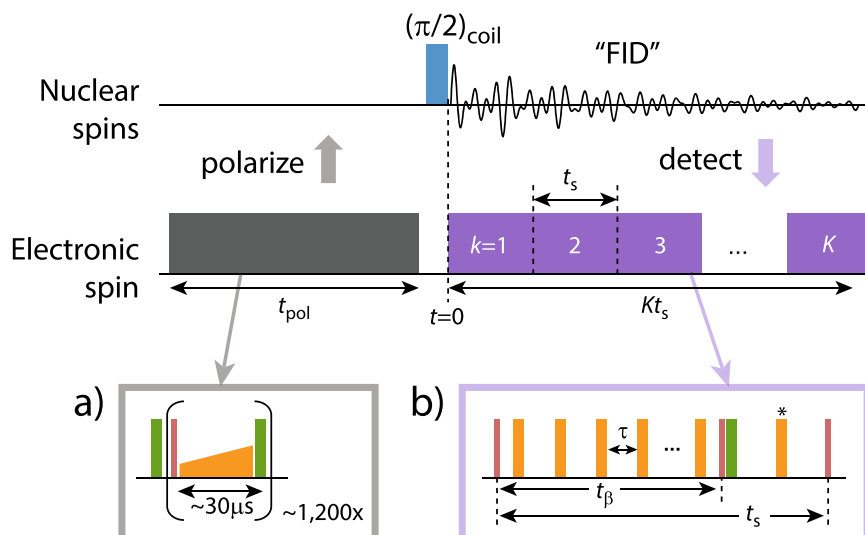
Fig. 2 Weak-measurement protocol for detecting the free precession signal from many nuclei in parallel. We polarize the nuclear spins by a repeated NOVEL sequence (gray, inset **a**)[87,88], initiate simultaneous precession of all nuclei by applying a $\pi/2$ pulse with an external RF coil (blue)[62], and detect the precession by repeated sampling of the transverse nuclear magnetization (purple)[17,18,89]. t_{pol} is the polarization time, t_s is the sampling time and K is the number of samples. Each weak-measurement read-out block (inset **b**) consists of a Carr–Purcell–Meiboom–Gill (CPMG) pulse train[90-92] of $4-24$ equidistant π pulses (orange) separated by a delay time $\tau = 1/(2\gamma_n B_0)$, followed by an optical read-out pulse (green). Red blocks are $\pi/2$ pulses. The duration of the CPMG sequence defines the interaction time t_β. An additional π pulse (*) is used to average over the electronic $m_S = 0, -1$ states. See the Supplementary Information for the full-timing diagram and experimental parameters.

not associated with the read-out process, such as spin-lattice effects or unresolved nuclear-nuclear couplings.

Finally, the azimuth ϕ_i is encoded in the complex phase of the nuclear FID signal. Because we initiate the FID by applying a $\pi/2$ pulse with an external RF coil, all nuclei are rotated around a common laboratory-frame axis and start precession with the same phase. By contrast, the ac detection of the FID is phase-sensitive with respect to each nucleus' individual hyperfine field. As a consequence, the phase ϕ_i is equal to the spatial angle between the coil and hyperfine axes in the laboratory frame (Fig. 1b)[21,22]. Analysis of the complex FID signal therefore directly reveals the desired azimuth ϕ_i.

In the following, we will make three important assumptions that are necessary for keeping the maximum likelihood fitting of spectra tractable. First, we assume that all nuclei carry approximately the same polarization, $p_{0,i} \approx p_0$. Because we repeat the polarization transfer process for typically $>10^3$ cycles (i.e., longer than the FID duration), we expect that all nuclei within the sensitive radius become close to fully polarized. The polarization level may be slightly reduced for spin pairs[55] or due to residual spin diffusion, however, these effects are small for our dilute ^{13}C concentration. Our assumption of nearly full polarization is consistent with the observation that spectra show little change in peak intensities once the number of cycles is increased beyond $\gtrsim 10^3$ [36]. Similar saturation behavior is suggested by ref. [52]. Second, we treat $T_{2,i}^* \approx T_2^*$ as a global parameter. Although this assumption is likely wrong in general, the role of T_2^* here is that of an upper bound in the FID decay. Because the FID is for most spins dominated by the measurement-induced dephasing (i) and (ii), our method is not very sensitive to variations in T_2^*. We find that our fit results for T_2^* are similar to those expected from the drift in the bias field, suggesting that our linewidths are limited by external field stability. Third, we will neglect nuclear-nuclear couplings, discussed further below.

Sensitive slice. The magnitude of the FID signal strongly depends on a spin's three-dimensional position $\mathbf{r}$, because of the position

dependence of the hyperfine interaction. We can capture the spatial dependence by calculating a sensitivity function $\mathcal{S}(\mathbf{r})$ that quantifies the signal contribution as a function of spin location $\mathbf{r}$. The sensitivity function is expressed as a signal-to-noise ratio and given by:

$$\mathcal{S}(\mathbf{r}) \equiv \mathcal{S}(\beta(\mathbf{r})) = \frac{A(\beta)}{\Gamma(\beta)t_s\sqrt{K}} \frac{(1 - e^{-\Gamma(\beta)Kt_s})}{\sqrt{t_{pol} + Kt_s}} \qquad (6)$$

where $\beta = a_\perp t_\beta / \pi$ (Eq. (3)) encodes the spatial position (via the hyperfine parameter $a_\perp$), and where K, t_s, t_β, and t_{pol} are experimental parameters defined in Fig. 2.

Figure 3 plots $\mathcal{S}(\mathbf{r})$ as a function of vertical and radial distance to the central electronic spin. Interestingly, the sensitivity does not monotonically decay with distance, as might be expected from the $a_\perp \propto r^{-3}$ scaling of the hyperfine interaction. Rather, $\mathcal{S}$ is initially low, and increases with r until it reaches a maximum at a characteristic radius r_{slice} before showing the expected r^{-3} decay. The suppression of signal from close spins is a consequence of quantum back-action[36]: Because these spins are strongly coupled, their measurement strength parameter β is large, leading to a rapid signal decay $1/\Gamma(\beta) \propto \beta^{-2} \to 0$ (Eq. (5b)). Conversely, distant spins with small β generate weak signals because $A(\beta) \to 0$ (Eq. (5a)). Maximum sensitivity results at an intermediate value where the two effects are balanced,

$$\beta^{(opt)} \approx \frac{2}{\sqrt{K}}. \qquad (7)$$

The optimum point of sensitivity is approximately reached when intrinsic and induced decay rates are commensurate, $(T_{2,n}^*)^{-1} = \beta^2/(4t_s)$ and when the FID record length is matched to the decay rate, $Kt_s = 1/\Gamma$.

As shown in Fig. 3, the points of maximum sensitivity are located along a contour of constant $a_\perp = \pi\beta^{(opt)}/t_\beta$. We denote this contour as the "sensitive slice" associated with the interaction time t_β. By varying t_β, we can vary the radius of the sensitive slice r_{slice} and tune detection from close to distant nuclear spins (Fig. 3, left to right). Because $a_\perp \propto r^{-3}$, the radius of the sensitive slice
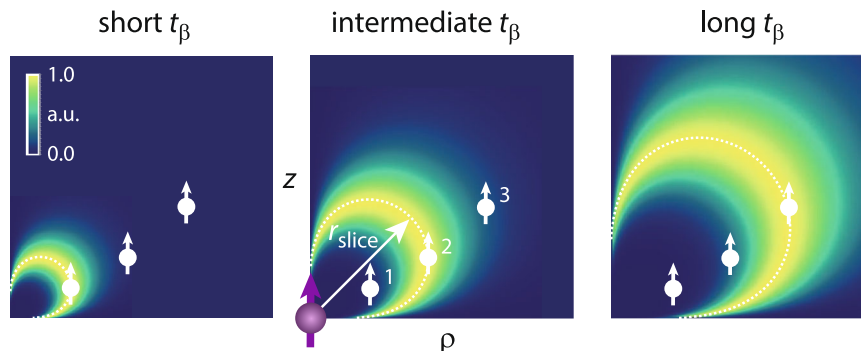
Fig. 3 Simulation of the sensitive slice $\mathcal{S}(\mathbf{r})$. ρz-plot of the sensitive slice for different interaction times t_β, where $z = r\cos\vartheta$ and $\rho = r\sin\vartheta$ are vertical and radial distance, respectively. Bright shading color codes the signal-to-noise ratio. By varying t_β the sensitive slice can be tuned to spins in close (1), intermediate (2), or far (3) distance from the central electronic spin (panels from left to right). The dashed contour is the $a_\perp$ isoline where $\beta = \beta^{(\text{opt})}$. r_{slice} is the characteristic radius of a slice. Plots assume $t_\ell = 0$ and $(T^*_{2,\text{n}})^{-1} = 0$.

scales as $r_{\text{slice}} \propto t_\beta^{1/6}$. The spatial selectivity is an important feature of our method, since it allows us to selectively probe nuclear spins at a defined (far) distance from the central electronic spin while avoiding interference from strongly-coupled nuclei in close proximity. Further, by sweeping t_β, we can collect FID traces from several sensitive slices and cover an extended spatial volume in the sample.

Maximum likelihood estimation by simulated annealing. Armed with a protocol for measuring the signals and coupling constants from many nuclei in parallel, we develop a maximum likelihood protocol to extract the hyperfine parameters and position vectors from an FID trace (Eq. 2).

We begin by setting up a likelihood model. Assuming n spins are contributing to the signal, our model contains $M = 3n + 3$ unknown parameters, including the three hyperfine parameters $a_{\parallel,i}$, $a_{\perp,i}$, and ϕ_i for each spin i plus three additional, global parameters accounting for an initial polarization p_0 and dephasing times $T^*_{2,\text{n}}$ and t_ℓ [see Eq. (5)]. Note that because the number of spins n is a priori unknown, M is itself a free parameter. To proceed, we collect the unknown parameters in the parameter vector $\boldsymbol{\theta} = \{\theta_m\}$, where $m = 1 \ldots M$. Our goal is to balance goodness of the fit and model complexity by minimizing a cost function of the form:

$$\text{IC} = G(\boldsymbol{\theta}, \mathbf{x}) + P(K, M), \tag{8}$$

where $G(\boldsymbol{\theta}, \mathbf{x})$ is a measure of the goodness of the fit, $\mathbf{x} = \{x_k\}$, where $k = 1 \ldots K$, is the set of measured data points, and $P(K, M)$ is a penalty term to prevent over-fitting[56]. Eq. (8) is the generic form of a so-called information criterion (IC). In our likelihood framework, $G(\boldsymbol{\theta}, \mathbf{x})$ can be expressed in terms of a negative likelihood function[57]:

$$G(\boldsymbol{\theta}, \mathbf{x}) = -2\ln(\mathcal{L}[\boldsymbol{\theta}, \mathbf{x}]) = K\ln\left(\sum_{k=1}^{K} [x_k - \tilde{x}_k(\boldsymbol{\theta})]^2\right), \tag{9}$$

where the argument of the logarithm is the residual sum of squares. The function $\tilde{x}_k(\boldsymbol{\theta})$ represents the estimated data points calculated from Eq. (2) using the parameter vector $\boldsymbol{\theta}$. For the penalty term $P(K, M)$, we choose the so-called weighted-average information criterion (WIC)[58] that is a weighted average of the Akaike and Bayesian information criteria (AIC[59] and BIC[60], respectively, see (See Supplementary Materials accompanying this manuscript for definition). The advantage of the WIC is that it performs well regardless of sample size K.

Minimization of Eq. (8) is highly nontrivial, as the number of fit parameters is large and M is itself an unknown. In this work, we

implement generalized simulated annealing (GSA)[38,39,61] algorithm to address this challenge. GSA is well-posed in our case because it works well for the global optimization of complicated, multi-dimensional systems with large numbers of local minima. To further improve the GSA, we run the minimization over a large number of random starting configurations for $\boldsymbol{\theta}$. Finally, once a best-estimate (lowest IC) set of parameters has been found, we compute the three-dimensional locations $\mathbf{r}_i$ of nuclei from the hyperfine vector $\mathbf{a}_i$ by inverting Eq. (1) (see Eqs. (10, 11) in the Methods).

Experimental demonstration. We experimentally demonstrate our three-dimensional nuclear localization strategy by imaging the ^{13}C environment of shallow NV centers in diamond. We focus on two NV centers in this work, labeled NV1 and NV2, out of five recorded datasets. The two NV centers are selected for favorable optical contrast and electron spin coherence times, but not for their ^{13}C environment. Their shallow depth (~10 nm) is not important for this study except for demonstrating that our method is compatible with near-surface NV centers. We probe the NV centers at room temperature using non-resonant optical excitation and a single-photon counting module. Electronic and nuclear spins are manipulated via two arbitrary waveform generators connected to a separate microwave transmission line and RF micro-coil circuits, respectively[21,62]. Experiments use a bias field $B_0 \sim 200$ mT aligned to within 1° of the NV symmetry axis (Fig. 1b). A description of diamond samples and the experimental setup is provided in the Methods section.

Figure 4a shows an example of an FID time trace from NV2 for $t_\beta = 4.944\ \mu$s, and Fig. 4b, c shows the complete dataset of ^{13}C Fourier spectra obtained for both NV centers. For each NV center, we record four spectra with different values of the interaction time t_β to sample different radii of the sensitive slice and to add redundancy. For each dataset, we plot the power spectrum, the real and imaginary parts of the complex Fourier spectrum, as well as the fit residues. Clearly, the spectra show a rich peak structure, indicating that we are detecting a large number of ^{13}C resonances.

To fit the spectra, we add the likelihood functions [Eq. 9] from all four spectra and minimize the total cost function [Eq. 8] using a single set of hyperfine parameters. We begin by randomly initializing each parameter, and then minimize the residues between the experimental and computed spectra using a GSA algorithm on a high-performance computer cluster[63]. To improve robustness, we fit the spectra, rather than the FID traces. We compute separate residues for real and imaginary parts of the complex spectrum as well as for their magnitude squared and minimize the sum of all residues. Additionally, we penalize
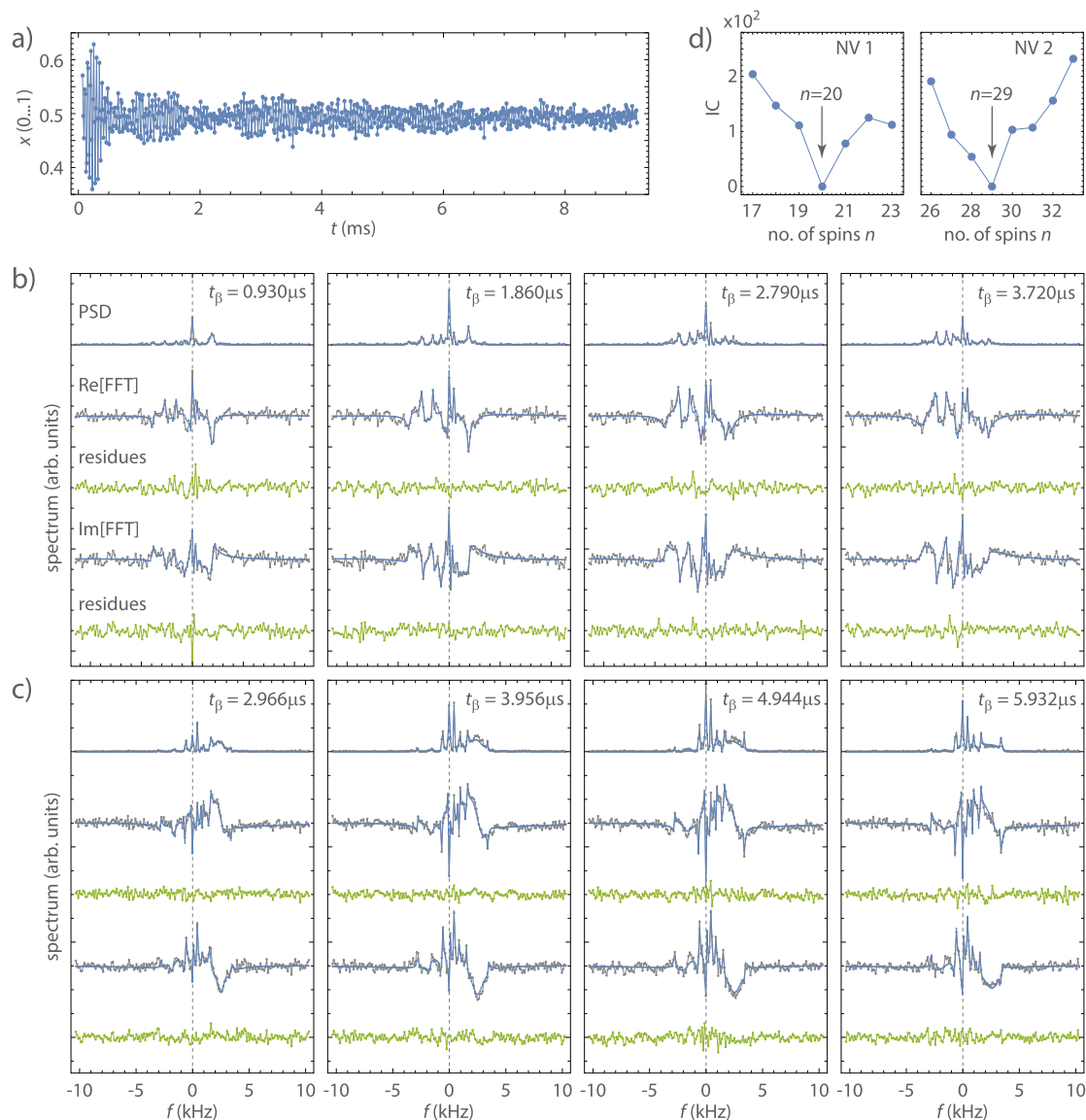
Fig. 4 Experimental demonstration of ^{13}C NMR spectroscopy of large spin clusters. a Example FID trace from NV2. Each data point reflects the probability amplitude $x(t)$ from one read-out block, integrated over ~10^6 repetitions of the full sequence (see Fig. 2). Measurement parameters are $t_{pol} = 40$ ms, $t_s = 11.48\,\mu s$, $t_\beta = 4.944\,\mu s$ and $K = 800$, and total measurement time is 11 h. **b** Complex Fourier spectra of the ^{13}C environment of NV1 for a series of interaction times t_β. Shown are from top to bottom (vertically offset for clarity): power spectrum (PSD), real part of the complex spectrum (Re[FFT]), fit residues for Re[FFT], the imaginary part of the complex spectrum (Im[FFT]), and fit residues for Im[FFT]. Blue traces are best fits (see text). The horizontal axis shows the spectral shift relative to the ^{13}C Larmor frequency at 2.156 MHz calibrated using correlation spectroscopy[54]. The bias field is $B_0 = 201.29$ mT. The PSD data of NV1 are the same as in ref. [36], Extended Data Fig. 5a. **c** Fourier spectra of the ^{13}C environment of NV2. Bias field is $B_0 = 188.89$ mT. **d** Cost function (IC, Eq. (8)) plotted as a function of the number of spins n. Best fits are obtained for $n = 20$ (NV1) and $n = 29$ (NV2). Since only differences in the cost function are meaningful, the minimum of the IC has been set to zero.

configurations where the distance between any two ^{13}C is less than one bond length. To accelerate the search for a global minimum, we repeat the procedure for a large number (~10^2) of starting values randomly chosen from predefined parameter intervals. Finally, to determine the number of spins we run the minimization routine for different n and select the configuration with the smallest global IC value (Fig. 4d). Once the minimization has terminated and n has been determined, we perform bootstrapping on the final fit residues[64] to obtain an estimate for the fit uncertainties for all parameters.

The calculated spectra for the most likely nuclear configurations are displayed as blue solid lines in Fig. 4b, c. For the two datasets, we find $n = 20$ for NV1 and $n = 29$ for NV2 (Fig. 4d).

The large IC >10 of the next-best configurations $n \pm 1$ indicates that our n are well-defined. (An IC >10 is equivalent to an evidence ratio of $e^{0.5IC} > 10^2$, meaning that our estimated n is $>10^2$ more likely than neighboring $n \pm 1$.) This statistical finding is supported by the good agreement between fit and experimental data (gray dots) and the small residues (green), which are of the same order as the measurement noise. We have verified the calculated spectra by performing a full density matrix simulation using the final parameter set (Fig. S2). All fit results are collected in Tables S3 and S4.

Figure 5 shows visualizations of the three-dimensional locations of nuclei. We find that nuclear positions are clustered between ca. $r = 0.7$–2.4 nm and ca. $\vartheta = 30$–75°. This clustering is
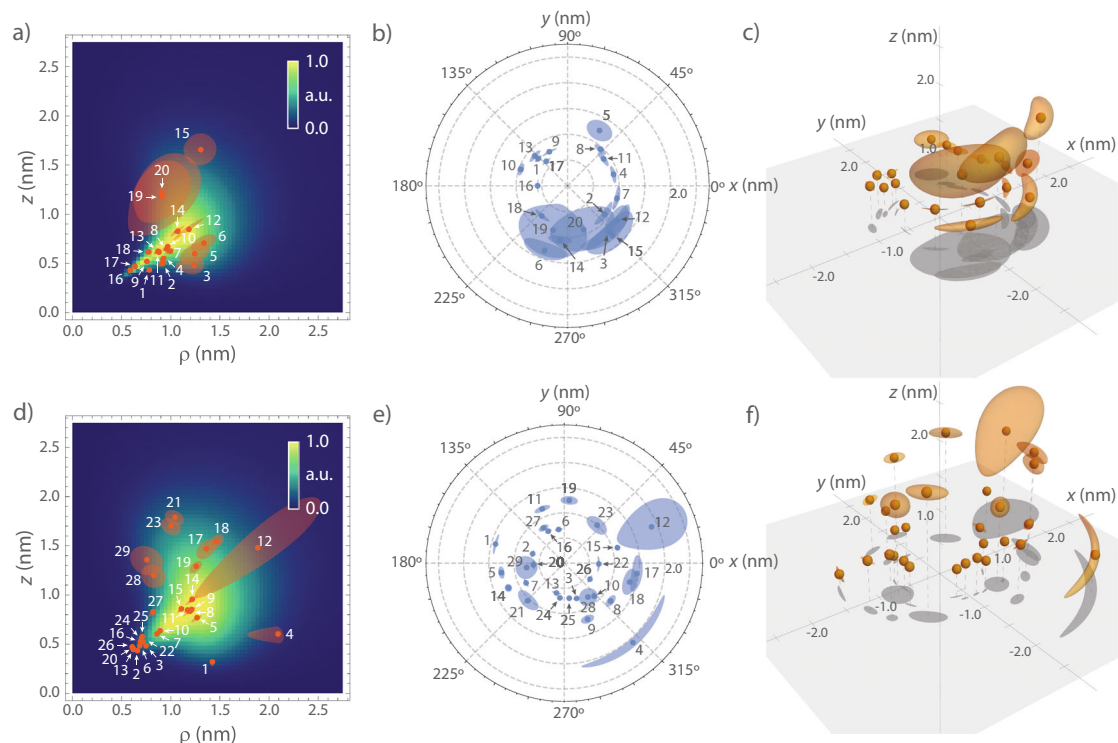
Fig. 5 Visualizations of the three-dimensional nuclear spin mapping. a Fitted spatial locations of the ^{13}C spins of NV1 (dots) shown in a ρz-plot. The central NV spin is located at the origin. Note that our method is ambiguous with respect to an inversion at the origin. Therefore, all nuclei are plotted in the upper hemisphere. Color coding reflects the combined sensitive slice [Eq. (6)] taking all t_β values as well as finite t_ℓ and $T^*_{2,n}$ into account. **b** Polar plot showing the azimuth ϕ on the xy-plane. **c** Three-dimensional view of the nuclear positions. **d–f** Corresponding plots for the carbon spins of NV2. Uncertainties (±1 standard error) are shown as shaded areas or volumes, respectively, and are omitted if smaller than the data points. Index labels refer to Tables S3 and S4 in the Supplementary Information.

a consequence of the spatial selectivity of our method: although the ^{13}C nuclei are distributed randomly over the diamond lattice, only spins falling within the sensitive slice are picked up by the weak-measurement detection sequence. Proximal spins ($r < 0.7$ nm) could be detected by further reducing t_β or by employing techniques developed for strongly-coupled nuclei[19,20]. More distant spins ($r > 2.4$ nm) can be addressed by increasing t_β, up to a limit set by the electronic coherence time $T_{2,e}$.

We find that the combined sensitive slice for all measurements (color-coded in Fig. 5a, d), taking the t_β values of the four spectra, t_ℓ and $T^*_{2,n}$ dephasing into account, agrees well with the extracted ^{13}C positions. (The t_ℓ dephasing suppresses signal from nuclei with large $a_{||}$, leading to low sensitivity for spins near $\vartheta = 0°$ and 90°). Figure 5 also clearly shows that the spatial precision of our method is highest and well below 1 Å for ^{13}C's that are located near the maximum of the sensitive slice, while the precision can be poor for spins located at the fringe of the slice.

The solution presented in Fig. 5 is a maximum likelihood estimate based on the assumptions of global values for the polarization and intrinsic dephasing as well as an absence of nuclear-nuclear couplings (see Section "Hyperfine parameters"). Our solution represents the three-dimensional nuclear spin configuration that has the highest likelihood, but there is no guarantee that it represents the "true" configuration of ^{13}C nuclei on the diamond carbon lattice. This probabilistic aspect is a standard feature of large-scale structure determination[65]. For example, because our method does not account for nuclear couplings, it is possible that spin pairs or clusters of ^{13}C are erroneously assigned a single-spin position. In addition, because of the inversion symmetry of the dipolar interaction [Eq. (1)], our method does not discriminate between spins lying in the upper

and lower hemisphere. Looking forward, this ambiguity will be naturally lifted for outside molecules. Further, both issues can be alleviated by introducing additional spatial constraints, especially by measuring nuclear spin-spin distances using two-dimensional NMR spectroscopy[27] (see Discussion).

To verify the three-dimensional nuclear configuration, we perform a set of basic statistical tests on the density, spatial distribution, and fit uncertainty of ^{13}C positions. Comparing the volume uncertainties δV of the ^{13}C (indicated by orange shading in Fig. 5c, e and tabulated in Supplementary Materials accompanying this manuscript.) with the volume per carbon atom in the diamond lattice ($V = 5.67$ Å^3 [66]), we find that 13 out of 20 spins (NV1) and 21 out of 29 spins (NV2) have $\delta V < V$ and therefore likely represent single nuclei. Next, defining the volume of the sensitive region by the volume in space contributing 50% to the total signal[10], we find sensitive volumes of $V = 9.3$ nm^3 and 14.8 nm^3 for NV1 and NV2, respectively. Considering an average density $\rho(^{13}C) = 1.94$ nm^{-3} for ^{13}C nuclei in diamond at natural isotope abundance (1.1%), the average number of ^{13}C in the sensitive slices are 18.0 and 28.6, respectively, in good agreement with our experimental result. Further, a χ^2 test for the angular distributions of the azimuth angles yields p-values well above the 5% level (54 and 70%, respectively), as expected for a random ^{13}C distribution. Within these statistics, our experimental results are fully consistent with a stochastic distribution of ^{13}C atoms around the NV centers. Finally, the $r > 0.7$ nm in retrospect justifies neglecting the Fermi contact interaction in our model[20,50].

Discussion

We conclude with a roadmap for extending the present experiment to samples outside of diamond, including individual
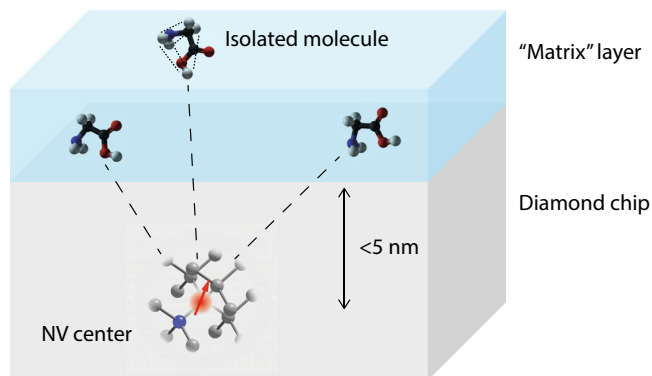
Fig. 6 Proposed strategy for single-molecule MRI. A few molecules of interest are immobilized on a diamond surface containing <5-nm-deep NV centers. Molecules are protected by a spin-free "matrix" layer (blue shading). The global position and conformation of molecules are imaged by our weak-measurement localization scheme (dashed lines), while precise local distances between nuclei are measured using two-dimensional NMR (dotted lines). Computational analysis is used to extract three-dimensional atomic coordinates.

molecules and complex spin structures (Fig. 6). Reaching this ambitious goal requires overcoming four central challenges:

(i)   To image outside nuclear spins, near-surface NV centers are needed. Although our scheme is compatible with near-surface NV centers, their properties are known to degrade. The degradation manifests itself both in a reduced coherence time and reduced stability of the negative NV charge state. Recently, there has been remarkable progress in stabilizing very shallow NV centers. In particular, ref. [67] reports coherence times of $T_{2,e} \sim 40\,\mu s$ for 5-nm-deep NV centers. In our experiments, we find similar values ($T_{2,e} \sim 50\,\mu s$ for a 3.5-nm-deep NV center). Extrapolating the $r \sim 2.4$ nm for ^{13}C (#12) in Fig. 5 using the $r \propto \gamma_n^{1/3} t_\beta^{1/6}$ scaling of the sensitive radius, the above $T_{2,e}$ implies a maximum radius of ca. 5–6 nm for single ^{1}H or ^{19}F nuclei (see Suppl. Fig. S5). This radius is compatible with the above shallow NV centers.

(ii) Single molecules must be immobilized and isolated on the diamond surface. This step can be achieved using surface functionalization[5,48,68]. To further protect the molecules and inhibit diffusion, molecules may be embedded in a spin-free matrix layer (Fig. 6)[69].

(iii) Nuclear spins in molecules will behave differently from internal ^{13}C nuclei. In particular, nuclear spin interactions will likely dominate over the hyperfine interaction. Nuclear spin interactions can be mitigated by homo- and hetero-nuclear decoupling techniques[70] and by isotope dilution[71]; however, they also are an important resource for structural information and a central element in our molecular imaging strategy, see next point.

(iv) Advanced spectroscopy and imaging techniques are needed that can efficiently retrieve the desired structure. A promising strategy is to combine the global distance information available by our scheme with local distance constraints obtained by solid-state NMR methods[27] (dashed and dotted lines in Fig. 6). For example, two-dimensional spectroscopy[9,25,72] and double-echo techniques[27,73] can be conveniently integrated with our protocol, because of its similarity to conventional FID detection. Additionally, efficient computational methods will be required to speed up data analysis and optimally extract the desired spatial information, including, for example, sparse sampling[29,74], gradient Monte Carlo[75], and machine learning techniques[76–78].

By demonstrating three-dimensional mapping of nuclear spins in ambient conditions, our work takes an important step forward towards the ambitious goal of single-molecule MRI. Looking beyond the milestone of structural imaging, the technique could be extended to study chemical binding and chemical surface reactions at the single-molecule level. For example, in a biological context, surface NMR may allow investigation of a priori unknown substrate binding sites in enzymes[79], as well as conformational changes in biomolecules associated with allosteric regulation[80], protein aggregation[81], or aptamer-target recognition[82]. These applications are particularly appealing because NMR can provide complementary information to other surface-sensitive techniques, such as surface-enhanced Raman spectroscopy (SERS), photoelectron spectroscopies, and fluorescence microscopy.

Besides magnetic imaging of single spins, our work also provides interesting perspectives for the characterization of large qubit registers in quantum applications. For example, our method can be applied to efficiently map out the coupling network of quantum nodes built from a central electronic spin backed by a nuclear spin register[83,84]. Such quantum nodes are central elements in emerging optical[85] or electronic[86] quantum interconnects. Another application is a nuclear quantum simulation using an electronic qubit for initialization and readout[40]. Finally, our parallel measurement protocol could provide a rapid means for calibrating cross-talk in superconducting qubit architectures[43,44].

Methods

Diamond samples. Two single-crystal diamond plates were used for experiments. Both sample A (NV1) and sample B (NV2) were electronic-grade, natural abundance (1.1% ^{13}C) diamond membranes. NV centers were created by ^{15}N$^+$ ion implantation at an energy of 5 keV and doses of 5×10^{11} cm^{-2} and 4×10^{10} cm^{-2} for samples A and B, respectively. Samples were subsequently annealed at 850 °C to form NV centers. We chose the ^{15}N species to discriminate implanted NV centers from native (^{14}N) NV centers. Both samples were cleaned in a 1:1:1 mixture of H$_2$SO$_4$:HNO$_3$:HClO$_4$ and baked at 465 °C in the air before mounting them in the setup. Whenever organic contamination was spotted, samples were cleaned in a 2:1 mixture of H$_2$SO$_4$:H$_2$O$_2$ (Piranha). We etched nano-pillars into the membrane surfaces to increase the photon collection efficiency. The continuous wave (CW) photon count rate was 250–500 kC/s.

Experimental setup. Experiments were performed using a custom-built confocal microscope equipped with a green $\lambda = 532$ nm frequency-doubled Nd:YAG excitation laser (CNI Laser MSL-FN-532nm) and a 630−800 nm detection path using a single-photon avalanche photodiode (APD, Pelkin Elmer SPCM-AQR Series). Optical pulses were generated by an acousto-optic modulator (AOM, Crystal Technology 3200-144) in a double-pass configuration, and gating of arriving photons was realized by time-tagging (NI-PCIe-6363) and software binning of photon counts. Typical laser excitation powers were on the order of 100 μW.

We synthesized microwave pulses for manipulating the electronic spin using an arbitrary waveform generator (AWG, Tektronix AWG5012C) and up-converted them to ~2.5 GHz using a local oscillator (Hittite HMC-T2100) and a quadrature mixer (Marki microwave IQ1545). Pulses were subsequently amplified (Gigatronics GT-1000A) prior to delivery to the NV center using a coplanar waveguide (CPW) photo-lithographically defined on a quartz cover slip. The transmission line was terminated on an external 50 Ω load (Meca 490-2). We synthesized radio-frequency (RF) pulses for nuclear spin manipulation using an AWG (National Instruments PCI-5421) and subsequently amplified them (Mini-Circuits LZY-22+). The pulses were transmitted using a planar micro-coil connected in series with a 50 Ω termination (Meca 697-30-1). The measured micro-coil inductance was $L = 0.77\,\mu$H. The 50 Ω termination increased the rf-circuit bandwidth ($Q = L/R$) at the expense of efficiency (most power was dissipated in the load). The micro-coil circuit had a 3-dB-bandwidth of ~19 MHz. ^{13}C Rabi frequencies were typically around 25 kHz. A layout of the micro-coil arrangement is given in ref. [62].

We used a cylindrical samarium-cobalt permanent magnet (TC-SmCo, reversible temperature coefficient 0.001%/$^\circ$C) to create a bias field $B_0 \sim 190$ mT at the NV center location. To align B_0 with the NV symmetry axis, we adjusted the relative location of the permanent magnet by fitting it to a set of electron paramagnetic resonance (EPR) lines recorded at different magnet locations and subsequently by maximizing the CW photon count rate.

Tracking of magnetic field drifts. The net magnetic bias field drifted by typically a few μT, leading to variations in the EPR frequency of order ±100 kHz and variations in the ^{13}C Larmor frequency of order ±50 Hz. This limited the observed ^{13}C linewidths to ~100 Hz. Field drifts were the dominating source of line

broadening for the ^{13}C NMR. We continuously tracked and logged magnetic field drifts by measuring the EPR resonance of the NV center and periodically read-justed the microwave excitation frequency during the course of the experiment.

Hyperfine vector a and position r. The radius r and polar angle ϑ are computed from the parallel and transverse hyperfine parameters $a_{\|}$ and $a_{\perp}$ as follows (see ref. [54], Eq. S28 and S29):

$$\vartheta = \arctan\left\{\frac{1}{2}\left(-3\frac{a_{\|}}{a_{\perp}} + \sqrt{9\frac{a_{\|}^2}{a_{\perp}^2} + 8}\right)\right\}, \tag{10}$$

$$r = \left\{\frac{\mu_0 \gamma_e \gamma_n \hbar (3\cos^2\vartheta - 1)}{4\pi a_{\|}}\right\}^{1/3}. \tag{11}$$

Data availability

The data that support the findings of this study are available from the corresponding author upon request.

Code availability

The code that was used to perform the GSA minimization is available from the corresponding author upon request.

References

1. Degen, C. L., Poggio, M., Mamin, H. J., Rettner, C. T. & Rugar, D. Nanoscale magnetic resonance imaging. *Proc. Natl Acad. Sci. USA* **106**, 1313 (2009).
2. Rose, W. et al. High-resolution nanoscale solid-state nuclear magnetic resonance spectroscopy. *Phys. Rev. X* **8**, 011030 (2018).
3. Sidles, J. A. Noninductive detection of single-proton magnetic resonance. *Appl. Phys. Lett.* **58**, 2854 (1991).
4. Ziarek, J. J., Peterson, F. C., Lytle, B. L. & Volkman, B. F. Binding site identification and structure determination of protein-ligand complexes by nmr a semiautomated approach. *Methods Enzymol.* **493**, 241–275 (2011).
5. Liu, K. S. et al. Surface NMR using quantum sensors in diamond. *Proc. Natl. Acad. Sci. USA* **115**, e2111607119 (2022).
6. Glaeser, R. M. Cryo-electron microscopy of biological nanostructures. *Phys. Today* **61**, 48 (2008).
7. Garman, E. F. Radiation damage in macromolecular crystallography: what is it and why should we care. *Acta Cryst. D* **66**, 339–351 (2010).
8. Glenn, D. R. et al. High-resolution magnetic resonance spectroscopy using a solid-state spin sensor. *Nature* **555**, 351 (2018).
9. Smits, J. et al. Two-dimensional nuclear magnetic resonance spectroscopy with a microfluidic diamond quantum sensor. *Sci. Adv.* **5**, eaaw7895 (2019).
10. Mamin, H. J. et al. Nanoscale nuclear magnetic resonance with a nitrogen-vacancy spin sensor. *Science* **339**, 557–560 (2013).
11. Staudacher, T. et al. Nuclear magnetic resonance spectroscopy on a (5-nanometer)^3 sample volume. *Science* **339**, 561–563 (2013).
12. Loretz, M., Pezzagna, S., Meijer, J. & Degen, C. L. Nanoscale nuclear magnetic resonance with a 1.9-nm-deep nitrogen-vacancy sensor. *Appl. Phys. Lett.* **104**, 033102 (2014).
13. Jelezko, F. et al. Observation of coherent oscillation of a single nuclear spin and realization of a two-qubit conditional quantum gate. *Phys. Rev. Lett.* **93**, 130501 (2004).
14. Dutt, M. V. G. et al. Quantum register based on individual electronic and nuclear spin qubits in diamond. *Science* **316**, 1312 (2007).
15. Dreau, A., Spinicelli, P., Maze, J. R., Roch, J. & Jacques, V. Single-shot readout of multiple nuclear spin qubits in diamond under ambient conditions. *Phys. Rev. Lett.* **110**, 060502 (2013).
16. Muller, C. et al. Nuclear magnetic resonance spectroscopy with single spin sensitivity. *Nat. Commun.* **5**, 4703–4703 (2014).
17. Boss, J. M., Cujia, K. S., Zopes, J. & Degen, C. L. Quantum sensing with arbitrary frequency resolution. *Science* **356**, 837–840 (2017).
18. Schmitt, S. et al. Submillihertz magnetic spectroscopy performed with a nanoscale quantum sensor. *Science* **356**, 832 (2017).
19. Zhao, N. et al. Sensing single remote nuclear spins. *Nat. Nano.* **7**, 657 (2012).
20. Zopes, J. et al. Three-dimensional localization spectroscopy of individual nuclear spins with sub-angstrom resolution. *Nat. Commun.* **9**, 4678 (2018).
21. Zopes, J., Herb, K., Cujia, K. S. & Degen, C. L. Three-dimensional nuclear spin positioning using coherent radio-frequency control. *Phys. Rev. Lett.* **121**, 170801 (2018).
22. Sasaki, K., Itoh, K. M. & Abe, E. Determination of the position of a single nuclear spin from free nuclear precessions detected by a solid-state quantum sensor. *Phys. Rev. B* **98**, 121405 (2018).
23. Shi, F. et al. Sensing and atomic-scale structure analysis of single nuclear-spin clusters in diamond. *Nat. Phys.* **10**, 21–25 (2014).
24. Abobeih, M. H. et al. One-second coherence for a single electron spin coupled to a multi-qubit nuclear-spin environment. *Nat. Commun.* **9**, 2552 (2018).
25. Yang, Z. et al. Structural analysis of nuclear spin clusters via 2d nanoscale nuclear magnetic resonance spectroscopy. *Adv. Quant. Technol.* **3**, 1900136 (2020).
26. Aslam, N. et al. Nanoscale nuclear magnetic resonance with chemical resolution. *Science* **357**, 67–71 (2017).
27. Abobeih, M. H. et al. Atomic-scale imaging of a 27-nuclear-spin cluster using a quantum sensor. *Nature* **576**, 411–415 (2019).
28. Ajoy, A., Bissbort, U., Lukin, M. D., Walsworth, R. L. & Cappellaro, P. Atomic-scale nuclear spin imaging using quantum-assisted sensors in diamond. *Phys. Rev. X* **5**, 011001 (2015).
29. Kost, M., Cai, J. & Plenio, M. B. Resolving single molecule structures with nitrogen-vacancy centers in diamond. *Sci. Rep.* **5**, 11007 (2015).
30. Perunicic, V. S., Hill, C. D., Hall, L. T. & Hollenberg, L. A quantum spin-probe molecular microscope. *Nat. Commun.* **7**, 12667 (2016).
31. Wang, Z.-Y., Haase, J. F., Casanova, J. & Plenio, M. B. Positioning nuclear spins in interacting clusters for quantum technologies and bioimaging. *Phys. Rev. B* **93**, 174104 (2016).
32. Schwartz, I. et al. Blueprint for nanoscale NMR. *Sci. Rep.* **9**, 6938 (2019).
33. Bradley, C. et al. A ten-qubit solid-state spin register with quantum memory up to one minute. *Phys. Rev. X* **9**, 031045 (2019).
34. Neumann, P. et al. Single-shot readout of a single nuclear spin. *Science* **329**, 542–544 (2010).
35. Shields, B., Unterreithmeier, Q. P., de Leon, N. P., Park, H. & Lukin, M. D. Efficient readout of a single spin state in diamond via spin-to-charge conversion. *Phys. Rev. Lett.* **114**, 136402 (2015).
36. Cujia, K. S., Boss, J. M., Herb, K., Zopes, J. & Degen, C. L. Tracking the precession of single nuclear spins by weak measurements. *Nature* **571**, 230 (2019).
37. Pfender, M. et al. High-resolution spectroscopy of single nuclear spins via sequential weak measurements. *Nat. Commun.* **10**, 594 (2019).
38. Kirkpatrick, S., Gelatt, C. D. & Vecchi, M. P. Optimization by simulated annealing. *Science* **220**, 671–680 (1983).
39. Tsallis, C. & Stariolo, D. A. Generalized simulated annealing. *Phys. A Stat. Mech. Appl.* **233**, 395 – 406 (1996).
40. Cai, J. M., Retzker, A., Jelezko, F. & Plenio, M. B. A large-scale quantum simulator on a diamond surface at room temperature. *Nat. Phys.* **9**, 168–173 (2013).
41. Waldherr, G. et al. Quantum error correction in a solid-state hybrid spin register. *Nature* **506**, 204–207 (2014).
42. Wolfowicz, G. et al. Quantum 29si nuclear spins as a resource for donor spin qubits in silicon. *New J. Phys.* **18**, 023021 (2016).
43. Krinner, S. et al. Benchmarking coherent errors in controlled-phase gates due to spectator qubits. *Phys. Rev. Appl.* **14**, 024042 (2020).
44. Tsunoda, T., Bhole, G., Jones, S. A., Jones, J. A. & Leek, P. J. Efficient hamiltonian programming in qubit arrays with nearest-neighbor couplings. *Phys. Rev. A* **102**, 032405 (2020).
45. Christle, D. J. et al. Isolated electron spins in silicon carbide with millisecond coherence times. *Nat. Mater.* **14**, 160–163 (2015).
46. Iwasaki, T. et al. Germanium-vacancy single color centers in diamond. *Sci. Rep.* **5**, 12882 (2015).
47. Sukachev, D. et al. Silicon-vacancy spin qubit in diamond: a quantum memory exceeding 10 ms with single-shot state readout. *Phys. Rev. Lett.* **119**, 223602 (2017).
48. Lovchinsky, I. et al. Nuclear magnetic resonance detection and spectroscopy of single proteins using quantum logic. *Science* **351**, 836 (2016).
49. Lovchinsky, I. et al. Magnetic resonance spectroscopy of an atomically thin material using a single-spin qubit. *Science* **355**, 503 (2017).
50. Nizovtsev, A. P. et al. Non-flipping 13 c spins near an nv center in diamond: hyperfine and spatial characteristics by density functional theory simulation of the c 510 [nv]h 252 cluster. *New J. Phys.* **20**, 023022 (2018).
51. Colangelo, G., Ciurana, F. M., Bianchet, L. C., Sewell, R. J. & Mitchell, M. W. Simultaneous tracking of spin angle and amplitude beyond classical limits. *Nature* **543**, 525–528 (2017).
52. Broadway, D. A. et al. Quantum probe hyperpolarisation of molecular nuclear spins. *Nat. Commun.* **9**, 1246 (2018).
53. Gefen, T., Khodas, M., McGuinness, L. P., Jelezko, F. & Retzker, A. Quantum spectroscopy of single spins assisted by a classical clock. *Phys. Rev. A* **98**, 013844 (2018).
54. Boss, J. M. et al. One- and two-dimensional nuclear magnetic resonance spectroscopy with a diamond quantum sensor. *Phys. Rev. Lett.* **116**, 197601 (2016).

55. Villazon, T., Chandran, A. & Claeys, P. W. Integrability and dark states in an anisotropic central spin model. *Phys. Rev. Res.* **2**, 032052 (2020).

56. Knowles, H. S., Kara, D. M. & Atature, M. Demonstration of a coherent electronic spin cluster in diamond. *Phys. Rev. Lett.* **117**, 100802 (2016).

57. Burnham, K. P. & Anderson, D. R. *Model Selection and Multimodel Inference* (Springer, 2002).

58. Wu, T.-J. & Sepulveda, A. The weighted average information criterion for order selection in time series and regression models. *Stat. Probab. Lett.* **39**, 1–10 (1998).

59. Akaike, H. A new look at the statistical model identification. *IEEE Trans. Automat. Contr.* **19**, 716–723 (1974).

60. Schwarz, G. Estimating the dimension of a model. *Ann. Statist.* **6**, 461–464 (1978).

61. Szu, H. & Hartley, R. Fast simulated annealing. *Physics Lett. A* **122**, 157 – 162 (1987).

62. Herb, K., Zopes, J., Cujia, K. S. & Degen, C. L. Broadband radio-frequency transmitter for fast nuclear spin control. *Rev. Sci. Instrum.* **91**, 113106 (2020).

63. ETH Zurich. Euler cluster. https://scicomp.ethz.ch (2020).

64. Efron, B. Bootstrap methods: another look at the jackknife. *Ann. Statist.* **7**, 1–26 (1979).

65. Shen, Y., Delaglio, F., Cornilescu, G. & Bax, A. Talos+: a hybrid method for predicting protein backbone torsion angles from nmr chemical shifts. *J. Biomol. NMR* **44**, 213–223 (2009).

66. Shikata, S. et al. Precise measurements of diamond lattice constant using bond method. *Jpn. J. Appl. Phys.* **57**, 111301 (2018).

67. Sangtawesin, S. et al. Origins of diamond surface noise probed by correlating single-spin measurements with surface spectroscopy. *Phys. Rev. X* **9**, 031052 (2019).

68. Sushkov, A. et al. Magnetic resonance detection of individual proton spins using quantum reporters. *Phys. Rev. Lett.* **113**, 197601 (2014).

69. Mamin, H. J., Sherwood, M. H. & Rugar, D. Detecting external electron spins using nitrogen-vacancy centers. *Phys. Rev. B* **86**, 195422 (2012).

70. Slichter, C. P. *Principles of Magnetic Resonance* 3rd edn (Springer, 1990).

71. Loquet, A., Lv, G., Giller, K., Becker, S. & Lange, A. 13c spin dilution for simplified and complete solid-state nmr resonance assignment of insoluble biological assemblies. *J. Am. Chem. Soc.* **133**, 4722–4725 (2011).

72. Aue, W. P., Bartholdi, E. & Ernst, R. R. Two-dimensional spectroscopy. application to nuclear magnetic resonance. *J. Chem. Phys.* **64**, 2229 (1976).

73. Ludwig, C. & Viant, M. R. Two-dimensional j-resolved nmr spectroscopy: review of a key methodology in the metabolomics toolbox. *Phytochem Anal.* **21**, 22–32 (2010).

74. Mobli, M., Maciejewski, M. W., Schuyler, A. D., Stern, A. S. & Hoch, J. C. Sparse sampling methods in multidimensional NMR. *Phys. Chem. Chem. Phys.* **14**, 10835–10843 (2012).

75. Hu, X., Beratan, D. N. & Yang, W. A gradient-directed monte carlo method for global optimization in a discrete space: application to protein sequence design and folding. *J. Chem. Phys.* **131**, 154117–154117 (2009).

76. Aharon, N. et al. NV-center-based nano-NMR enhanced by deep learning. *Sci. Rep.* **9**, 17802 (2019).

77. Kong, X. et al. Artificial intelligence enhanced two-dimensional nanoscale nuclear magnetic resonance spectroscopy. *npj Quantum Inf.* **6**, 79 (2020).

78. Jung, K. et al. Deep learning enhanced individual nuclear-spin detection. *npj Quantum Inf.* **7**, 41 (2021).

79. Mistry, J., Bateman, A. & Finn, R. D. Predicting active site residue annotations in the pfam database. *BMC Bioinformatics* **8**, 298 (2007).

80. Gunasekaran, K., Ma, B. & Nussinov, R. Is allostery an intrinsic property of all dynamic proteins. *Proteins* **57**, 433–443 (2004).

81. Ross, C. A. & Poirier, M. A. What is the role of protein aggregation in neurodegeneration. *Nat. Rev. Mol. Cell Biol.* **6**, 891–898 (2005).

82. Nakatsuka, N. et al. Aptamer-field-effect transistors overcome debye length limitations for small-molecule sensing. *Science* **362**, 319 (2018).

83. Awschalom, D. D., Hanson, R., Wrachtrup, J. & Zhou, B. B. Quantum technologies with optically interfaced solid-state spins. *Nat. Photonics* **12**, 516–527 (2018).

84. Zwanenburg, F. A. et al. Silicon quantum electronics. *Rev. Mod. Phys.* **85**, 961–1019 (2013).

85. Bernien, H. et al. Heralded entanglement between solid-state qubits separated by three metres. *Nature* **497**, 86–90 (2013).

86. Tosi, G. et al. Silicon quantum processor with robust long-distance qubit couplings. *Nat. Commun.* **8**, 450 (2017).

87. Henstra, A., Dirksen, P., Schmidt, J. & Wenckebach, W. Nuclear spin orientation via electron spin locking (NOVEL). *J. Magn. Reson.* **77**, 389–393 (1988).

88. London, P. et al. Detecting and polarizing nuclear spins with double resonance on a single electron spin. *Phys. Rev. Lett.* **111**, 067601 (2013).

89. Degen, C., Reinhard, F. & Cappellaro, P. Quantum sensing. *Rev. Mod. Phys.* **89**, 035002 (2017).

90. Lange, G. D., Riste, D., Dobrovitski, V. V. & Hanson, R. Single-spin magnetometry with multipulse sensing sequences. *Phys. Rev. Lett.* **106**, 080802 (2011).

91. Alvarez, G. A. & Suter, D. Measuring the spectrum of colored noise by dynamical decoupling. *Phys. Rev. Lett.* **107**, 230501 (2011).

92. Kotler, S., Akerman, N., Glickman, Y., Keselman, A. & Ozeri, R. Single-ion quantum lock-in amplifier. *Nature* **473**, 61–65 (2011).

Acknowledgements

Author contributions

C.L.D. initiated the project. K.S.C. performed the experiments on a setup built by K.S.C. and K.H. K.S.C. developed the GSA minimization and analyzed the data. K.S.C. and C.L.D. co-wrote the paper with input from K.H., J.Z., and J.M.A. All authors discussed the results.

Competing interests

The authors declare no competing interests.

Additional information